Maximally stable lobed balloons

M. Pagitz [a], S. Pellegrino [b],*

[a] Aerospace Structures, Delft University of Technology, 2629 HS Delft, The Netherlands
[b] Graduate Aerospace Laboratories, California Institute of Technology, 1200 East California Boulevard, Pasadena, CA 91125, USA

ARTICLE INFO

ABSTRACT

This paper is concerned with the optimization of the cutting pattern of n-fold symmetric super-pressure balloons made from identical lobes constrained by stiff meridional tendons. It is shown that the critical buckling pressure of such balloons is maximized if the unstressed surface area of the balloon is minimized under a stress constraint. This approach results in fully stressed balloon designs that in some cases have a smaller unstressed surface area than the corresponding axisymmetric surface that is in equilibrium with zero hoop stress. It is shown that, compared to current designs, the buckling pressures can be increased by up to 300% without increasing the maximum stress in the lobe.

© 2010 Elsevier Ltd. All rights reserved.

1. Introduction

Lobed balloons have been chosen by NASA for the next generation of super-pressure balloons for long duration stratospheric missions. The shape of these balloons results from the pressurization of a thin plastic envelope, made of a linear low density polyethylene (LLDPE) film, contained within equally spaced meridional tendons, Fig. 1(a). This design exploits the high curvature of the lobes to reduce the forces in the envelope and so makes it possible to design balloons of larger diameter without having to increase also the thickness of the film, just by increasing the number of the meridional tendons.

However, it was discovered that balloons with a high degree of lobing – which is beneficial in reducing the maximum stress – are prone to buckling and it was then shown that lobed balloons have a critical uniform buckling pressure at which the n-fold symmetric inflated shape becomes unstable. An account of these developments has been presented by Pagitz and Pellegrino (2007) who went on to show that relatively small changes to the critical pressure could be made by changing the material parameters, including the Young's modulus of the film, the stiffness of the tendon, and the Poisson's ratio of the film, but order-of-magnitude changes could be achieved by changing the cutting pattern for the lobes from a constant angle (CA) to a constant radius (CR) design; see Fig. 2 for an explanation of these cutting patterns. The CA and CR patterns had been derived from simple geometric considerations;

the present paper will show that significant further improvements can be obtained from a mathematical optimization approach.

Starting from an extension of Pagitz and Pellegrino (2007), this research began by searching for the cutting pattern that maximizes the smallest eigenvalue of the tangent stiffness matrix of a balloon at a given uniform differential pressure p. It was found that these optimal cutting patterns lead to fully stressed balloon designs and thus correspond to balloons of minimal surface area, subject to a given stress constraint. Therefore, since minimizing the cutting pattern area is much faster than maximizing the smallest eigenvalue of the tangent stiffness matrix, the former approach was later adopted. Hence, the optimization technique and the solutions that will be presented in this paper are all based on this minimum area approach. Although there is no proof that these solutions correspond to the maximum critical pressures solution, by computing the critical pressure during the optimization it will be shown that there is a clear correlation between decreasing the surface area and increasing the critical pressure.

In addition to buckling under a uniform pressure, lobed balloons are prone to another kind of instability, which occurs when a balloon is inflated under a pressure gradient. This instability results in clefted shapes that appear to be stable; it will not be considered in the present paper. The interested reader is referred to, for example, Baginski et al. (2006), Schur and Jenkins (2002), Schur (2004), and Deng and Pellegrino (2008).

The paper is arranged as follows. Section 2 gives a formal definition of the optimization problem. Section 3 presents the shape functions that are used to describe the cutting pattern for a lobe of the balloon and Section 4 presents the optimization algorithm to minimize the unstressed lobe area, subject to a constraint on

---

* Corresponding author.
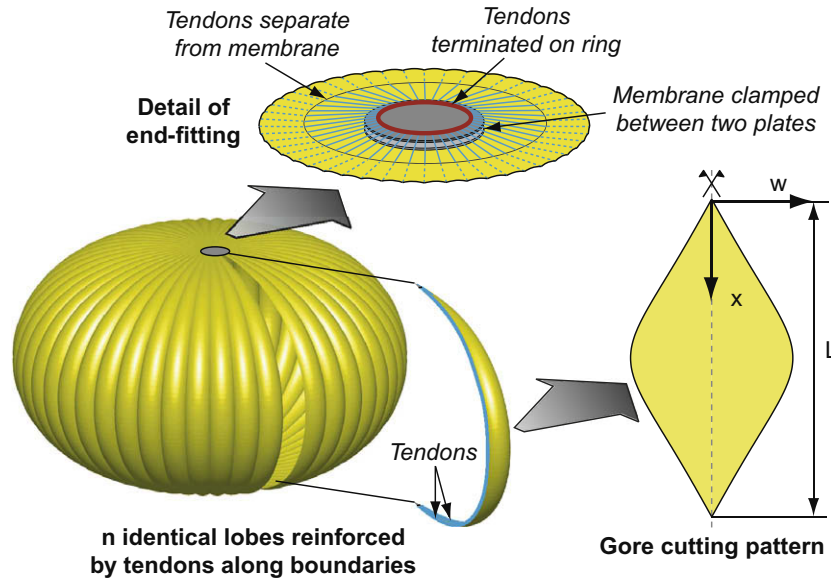 E-mail address: sergiop@caltech.edu (S. Pellegrino).

Fig. 1. Concept of lobed balloon and coordinate system for gore cutting pattern.

the maximum value of the Mises stress in the lobe, for a given differential pressure. Section 5 defines the geometry of two balloons, with diameters of 10 m and 80 m, and their material properties, assumed to be linear-elastic. Section 6 presents sets of optimized designs for these two balloon sizes, for different number of lobes. Section 7 concludes the paper.

2. Formulation of optimization problem

Consider a balloon made from n identical flat lobes. A general lobe cutting pattern is defined by the semi-width $w(x)$, expressed in terms of n polynomial shape functions, each multiplied by an amplitude $v(i)$, Fig. 1. The corresponding area of the unstressed lobe is

$$f(\mathbf{v}) = 2 \int_0^L w \, dx, \tag{1}$$

where $\mathbf{v} = [v_1, \ldots, v_n]$ and L is the total length of the centreline.

A stress constraint will be imposed by setting a limit on the maximum Mises stress in the lobe. When the balloon is loaded by a given uniform pressure p the Mises stress is denoted by

$$g(\mathbf{v}) = \sqrt{\sigma_1^2 + \sigma_2^2 - \sigma_1 \sigma_2}, \tag{2}$$

where σ_1, σ_2 are the principal stresses. This expression for the stress limit can take different functional forms, depending on the type of behavior that needs to be optimized, which in turn depends on the specific mission for which a balloon is designed. The present choice aims to minimize visco-elastic effects by imposing a limit on the effective stress that controls the creep rate. Eq. (2) is a simplified form of the effective stress proposed by Rand and Sterling (2006).

Hence, the area minimization problem can be stated as follows:

Minimize $f(\mathbf{v})$ subject to $g(\mathbf{v}) = \sigma_0$ where σ_0 is a given Mises stress.

3. Shape functions for cutting patterns

A general cutting pattern can be expressed in terms of shape functions based on Bernstein polynomials (Bernstein, 1912). The $n + 1$ Bernstein polynomials of degree n are defined as
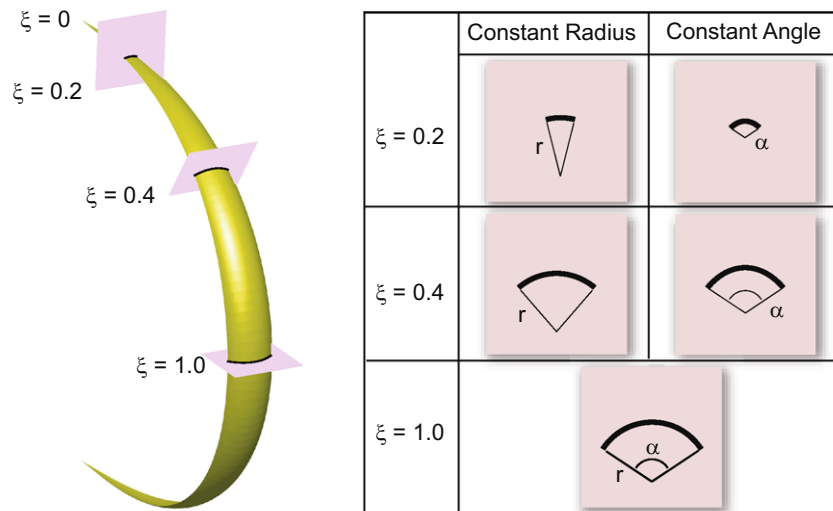

Fig. 2. Cross-sections of an inflated lobe.

$$B_{k,n}(\xi) = \binom{n}{k} \xi^k (1-\xi)^{n-k} \tag{3}$$

with $\xi \in [0,1]$; the binomial coefficient $\binom{n}{k}$ is

$$\binom{n}{k} = \frac{n!}{(n-k)!k!}. \tag{4}$$

Hence, the polynomials for $n = 0, 1, 2$ are, respectively

$$B_{0,0}(\xi) = 1; \quad \begin{cases} B_{0,1}(\xi) = 1-\xi \\ B_{1,1}(\xi) = \xi \end{cases}; \quad \begin{cases} B_{0,2}(\xi) = (1-\xi)^2 \\ B_{1,2}(\xi) = 2(1-\xi)\xi \\ B_{2,2}(\xi) = \xi^2 \end{cases}. \tag{5}$$

Fig. 3 shows plots of the polynomials of degree up to $n = 5$. Bernstein polynomials have a number of useful properties. In particular, they satisfy symmetry

$$B_{k,n}(\xi) = B_{n-k,n}(1-\xi) \tag{6}$$

and the sum of all polynomials of degree n is equal to 1, i.e.

$$\sum_{k=0}^{n} B_{k,n}(\xi) = 1. \tag{7}$$

A property that will be used to simplify the shape optimization is that the areas under the polynomials of degree n in the interval $\xi \in [0,1]$ are all equal. More formally

$$\int_0^1 B_{k,n}(\xi)\, d\xi = \int_0^1 \binom{n}{k} \xi^k (1-\xi)^{n-k}\, d\xi = \frac{1}{n+1} \tag{8}$$

from which it can be shown that the sensitivity of the lobe area with respect to the optimization variables is constant.

The profile of the cutting pattern can be expressed in terms of the above shape functions and of the amplitudes $v(i)$

$$w(\xi) = \sum_{k=0}^{n} \mathbf{v}_{k+1} B_{k,n}(\xi) \quad \text{for } \xi \in [0,1]. \tag{9}$$

Here it should be noted that, instead of the variable $x \in [0,L]$ defined over the full length of the lobe, we are using the non-dimensional variable ξ that is equal to 1 at the centre of the lobe, as shown in Fig. 2. Hence, $x = \xi L/2$. Assuming the lobe cutting pattern to have mirror symmetry with respect to the centre line $x = L/2$, only the upper half of the cutting pattern will be considered.

The objective $f(\mathbf{v})$ to be minimized can be expressed as follows:

$$f(\mathbf{v}) = 2 \int_0^L w\, dx = 2L \int_0^1 w(\xi)\, d\xi = 2L \sum_{k=0}^{n} \mathbf{v}_{k+1} \int_0^1 B_{k,n}(\xi)\, d\xi$$

$$= \frac{2L \sum_{k=0}^{n} \mathbf{v}_{k+1}}{n+1}. \tag{10}$$

Since the width of the lobe at the apex is zero

$$w(\xi = 0) = 0, \quad \text{hence } v_1 = 0. \tag{11}$$

Also, the slope at the mid-point is zero

$$w'(\xi = 1) = 0, \quad \text{hence } \frac{\partial w(1)}{\partial \xi} = \sum_{k=0}^{n} \mathbf{v}(k+1) \frac{\partial B_{k,n}(1)}{\partial \xi} = 0$$

$$\text{hence } v_n = v_{n+1}. \tag{12}$$

Using these conditions, it is possible to reduce the number of unknowns to $n - 1$.

In the present study, the value $n = 5$ was chosen and hence only the four shape functions shown in Fig. 4(a) are needed. Since $v_5 = v_6$, the fourth shape function has been taken as $B_{4,5} + B_{5,5}$. As an example, the decomposition of a CR cutting pattern into these four shape functions is shown in Fig. 4(b). Note that the original CR pattern has been approximated very accurately.

4. Optimization algorithm

Since the objective is linear, optimization algorithms based on second-order information are not applicable. A further requirement on the algorithm is that a non-linear maximum stress constraint has to be taken into account. The shape optimization and line search algorithms that have been implemented are presented in the following.

4.1. Method of feasible directions

A gradient based algorithm that is capable of dealing with highly non-linear constraints is chosen for the shape optimization. An algorithm that fits into this scheme is the Method of Feasible Directions (Zoutendijk, 1960). A version of this algorithm is presented in the following for n optimization variables and one constraint.
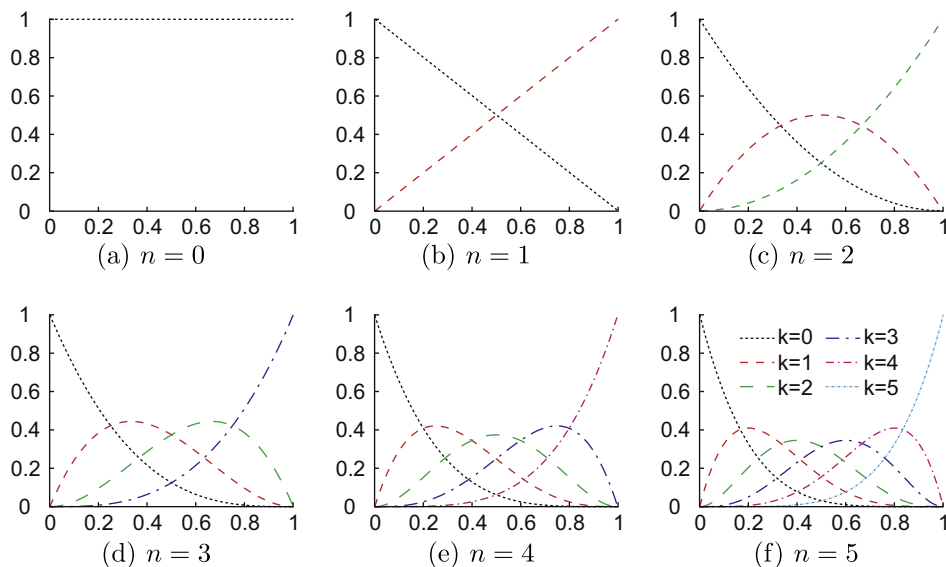

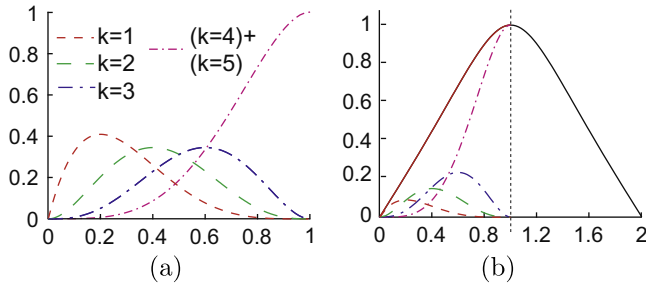
Fig. 3. Bernstein polynomials of degree $n \in [0,5]$.

Fig. 4. (a) Shape functions of degree $n = 5$ for shape optimization; (b) decomposition of CR cutting pattern with subtended angle of $118°$ at equator.

The gradients $\partial f / \partial \mathbf{v}$ and $\partial g / \partial \mathbf{v}$ can be written as

$$\frac{\partial f}{\partial \mathbf{v}} = \begin{bmatrix} \frac{\partial f}{\partial v_1} & \frac{\partial f}{\partial v_2} & \cdots & \frac{\partial f}{\partial v_n} \end{bmatrix}^T \quad \text{and} \quad \frac{\partial g}{\partial \mathbf{v}} = \begin{bmatrix} \frac{\partial g}{\partial v_1} & \frac{\partial g}{\partial v_2} & \cdots & \frac{\partial g}{\partial v_n} \end{bmatrix}^T. \tag{13}$$

The equation of an hyperplane passing through point $\mathbf{v}$, where the change in the objective is zero, can be written as

$$\Delta f = \frac{\partial f}{\partial \mathbf{v}}^T \Delta \mathbf{v} = \frac{\partial f}{\partial v_1} \Delta v_1 + \frac{\partial f}{\partial v_2} \Delta v_2 + \cdots + \frac{\partial f}{\partial v_n} \Delta v_n = 0 \tag{14}$$

and solving for Δv_n gives

$$\Delta v_n = - \frac{\frac{\partial f}{\partial v_1} \Delta v_1 + \frac{\partial f}{\partial v_2} \Delta v_2 + \cdots + \frac{\partial \mathbf{f}}{\partial v_{n-1}} \Delta v_{n-1}}{\frac{\partial f}{\partial v_n}}. \tag{15}$$

For movements in this hyperplane the gradient of the constraint results in

$$\Delta g = \frac{\partial g}{\partial v_1} \Delta v_1 + \cdots + \frac{\partial g}{\partial v_{n-1}} \Delta v_{n-1} - \frac{\frac{\partial g}{\partial v_n} \left(\frac{\partial f}{\partial v_1} \Delta v_1 + \cdots + \frac{\partial f}{\partial v_{n-1}} \Delta v_{n-1} \right)}{\frac{\partial f}{\partial v_n}}, \tag{16}$$

where Eq. (15) is introduced to keep the objective fixed. The direction where the constraint has a maximal gradient thus becomes

$$\frac{\partial \Delta g}{\partial \mathbf{v}} = \begin{bmatrix} \frac{\partial g}{\partial v_1} - \frac{\frac{\partial g}{\partial v_n} \frac{\partial f}{\partial v_1}}{\frac{\partial f}{\partial v_n}} & \cdots & \frac{\partial g}{\partial v_{n-1}} - \frac{\frac{\partial g}{\partial v_n} \frac{\partial f}{\partial v_{n-1}}}{\frac{\partial f}{\partial v_n}} & 0 \end{bmatrix}^T \tag{17}$$

and v_n can be obtained by inserting Eq. (17) into Eq. (15)

$$v_n = \frac{\frac{\partial g}{\partial v_n} \left(\frac{\partial f}{\partial v_1} \right)^2 + \cdots + \frac{\partial g}{\partial v_n} \left(\frac{\partial f}{\partial v_{n-1}} \right)^2 - \frac{\partial f}{\partial v_1} \frac{\partial f}{\partial v_n} \frac{\partial g}{\partial v_1} - \cdots - \frac{\partial f}{\partial v_{n-1}} \frac{\partial f}{\partial v_n} \frac{\partial g}{\partial v_{n-1}}}{\left(\frac{\partial f}{\partial v_n} \right)^2}. \tag{18}$$

Similar expressions for a hyperplane on which the constraint remains unchanged can be obtained by exchanging f with g. The directions of steepest descent for both hyperplanes are illustrated in Fig. 5 and it can be seen that they border a region that is usable – the objective is decreased or stays the same – and feasible – the constraint is decreased or stays the same – for vectors of infinitesimally small length that are located in this region.

Many different methods have been proposed to determine the angle of the direction with respect to the steepest descent in one of the hyperplanes. A detailed discussion and references to the major papers in this field can be found in Vanderplaats (2001). Throughout this paper, to simplify matters, the direction of the single iteration steps is located along the steepest descent of the hyperplanes. Starting from a feasible solution, the actual result is improved by moving in a direction in which the constraint is unchanged while the objective is improved. If the constraint is violated then the following iteration uses the other hyperplane
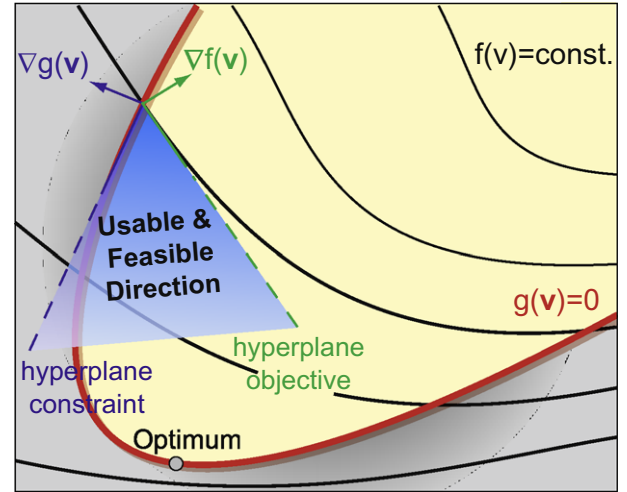

Fig. 5. Illustration of method of feasible directions.

that leaves the objective unchanged (for infinitesimally small displacements). Close to the optimum – defined by the Karush–Kuhn–Tucker condition (Karush, 1939; Kuhn and Tucker, 1951) – the directions of steepest descent of both hyperplanes become identical, hence the magnitude of their scalar product can be used as a convergence criterion.

4.2. Line search

The previous section has shown how to compute the direction of a new iteration step, however, the step length is still unknown. It can be determined with the help of so-called "line search algorithms", which are able to find an extremum of a function of one variable and also can find the value of the variable for which the function has a prescribed value. Two of the most popular line search algorithms have been considered; their advantages and drawbacks are discussed next.

Since the value of the function and its derivative are known from the optimization at the origin of the search vector, polynomial approximations are often an excellent choice to find an extremum with a minimum number of function evaluations. However, these methods have the disadvantage that the accuracy of the interpolations cannot be guaranteed and for highly non-linear problems it might be quite poor. Hence, the rate of convergence for methods that are based on curve-fitting is not known (Vanderplaats, 2001). The golden section method (Press et al., 2003) is another technique that is able deal with highly non-linear functions; furthermore, the rate of convergence is known.

Let $f(x)$ be a convex function with a minimum in the interval $x \in [0, 1]$; the function values $f(0)$ and $f(1)$ are known. If this interval is divided at a point $\xi | \xi \geqslant \eta = 1 - \xi$ with the function value $f(\xi)$ then the initial state of the line search as shown in Fig. 6 is
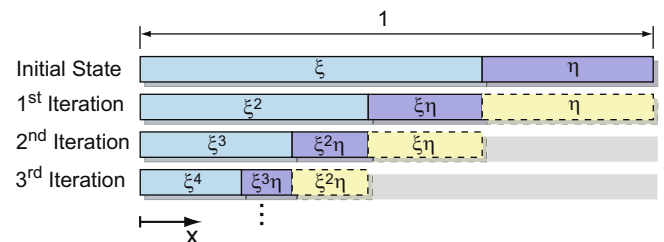

Fig. 6. Scheme of golden section method.

obtained. The function can only have a minimum in the given interval iff $f(\xi) < f(0) \wedge f(\xi) < f(1)$.

To determine a new, smaller interval that contains the minimum of the function it is necessary to compute a fourth value. The location of this value is chosen in the larger interval $[0, \xi]$ – to guarantee a better distribution – and is determined such that the ratio between the larger and smaller subinterval is again equal to ξ/η which results in $f(\xi^2)$ (see first iteration in Fig. 6). If $f(\xi^2) < f(\xi)$ then the minimum can be found in the interval $[0, \xi]$, if $f(\xi^2) > f(\xi)$ it is in the interval $[\xi^2, 1]$ and for $f(\xi^2) = f(\xi)$ both intervals contain the minimum. Assuming $\xi^2 + \xi\eta \geqslant \xi\eta + \eta$ then it is more likely that the minimum is located in the larger interval $[0, \xi^2 + \xi\eta]$. Fig. 6 shows, under the assumption that the minimum is always located in the larger subinterval, the next two iteration steps. Thus the length L of the subinterval after the nth iteration becomes

$$L \leqslant \xi^{n+1} + \xi^n\eta. \tag{19}$$

For the case where $\xi^2 = \eta$ the following convergence rate can be guaranteed:

$$L = \xi^{n+1} + \xi^n\eta. \tag{20}$$

Since $\xi + \eta = 1$ we finally get

$$\xi = \frac{-1 + \sqrt{5}}{2}; \quad \eta = \frac{3 - \sqrt{5}}{2} \tag{21}$$

such that

$$\chi = \frac{\xi}{\eta} = \frac{-1 + \sqrt{5}}{3 - \sqrt{5}} = \frac{1 + \sqrt{5}}{2} = 1.618033989\ldots \tag{22}$$

is the golden ratio.

4.3. Example

The performance of the golden section method and polynomial interpolation in finding the minimum of a highly non-linear function is investigated. The function is

$$f(x) = -1 - 20x + e^{6x}. \tag{23}$$

Fig. 7 shows the minimum of $f(x)$ together with the minima obtained from polynomial interpolations of degree $i \in [2\ldots4]$ that make use of the gradient $f'(0)$ and function values at $f(0)$ and $f(1)$. The remaining information needed for the interpolations is
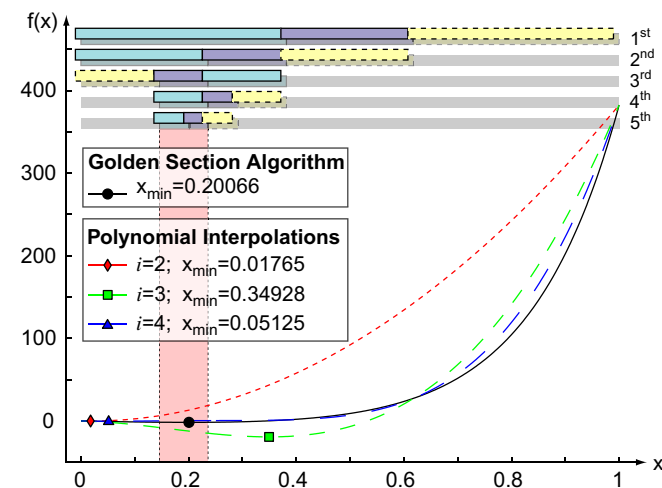
computed according to a grid that is identical to the one obtained by the golden section algorithm. It can be seen that the predicted minima are quite poor and clearly insufficient for an optimization algorithm. Furthermore, it has to be taken into account that increasing the polynomial degree is not advisable due to possible oscillations. In contrast, the first five iterations of the golden section method are shown at the top of Fig. 7. It is obvious that much better and more reliable results than from the polynomial interpolations are obtained. However, this comes at the cost of a larger number of function evaluations.

Hence, an algorithm that combines both methods is used in the following. In a first step, the interval that contains the minimum is sufficiently reduced by 10 iterations of the golden section method (which reduces the size of the original interval to 0.8%) and the minimum is finally approximated by a quadratic interpolation. It should be remarked that the golden section method can also be used to find a point where $f(x) = k$ by minimizing $|f(x) - k|$.

5. Geometric and material properties of balloons

The geometric and material properties of the pumpkin balloons that have been considered are presented in Table 1, where it should be noted that a reduced pseudo-elastic modulus has been provided for the film, to take visco-elastic effects into account. Identical balloons were studied by Pagitz and Pellegrino (2007). It should also be noted that the optimized cutting patterns are, in contrast to the CA and CR designs, a function of the geometry, the material parameters, and the maximum stress constraint.

6. Optimization results

6.1. Small scale balloons

Small scale balloons with a diameter of 10 m and different numbers of lobes $n \in \{16, 80, 145\}$ have been optimized. The optimization was done at a differential pressure of $p = 500$ Pa and the maximum allowed Mises stresses in the membrane were set equal to the maximum stresses that occur in a CR cutting pattern with a subtended angle of 118°. Furthermore, the initial geometry was obtained by a least square interpolation of the same CR cutting pattern. Note that the subtended angles of the optimized cutting patterns are not fixed but are in fact a result of the optimization itself.

The performance of the previously introduced optimization algorithm is demonstrated in Fig. 8 for a balloon with 145 lobes. It can be seen that a fully stressed configuration is obtained after

Fig. 7. Comparison between polynomial interpolation of degree i and golden section method in finding minimum of $f(x)$.

Table 1
Geometric and material properties of balloons under consideration.

|	Small balloons	Flight-size balloons
Geometric properties		
Number of lobes	16–145	290
Total height (m)	5.99	47.92
Diameter (to tendons) (m)	10.00	80.00
Total length of tendons (m)	13.11	104.88
Cutting pattern	CA and CR	CR
Lobe subtended angle at equator (°)	118	105
Radius of end-fittings (m)	0.29	0.70
Material properties		
Young's modulus of film (N/mm²)	138.70	214.00
Poisson's ratio of film	0.566	0.450
Thickness of film (mm)	0.038	0.048
Coefficient of thermal expansion of film	4×10^{-4}	4×10^{-4}
Axial stiffness of tendons (kN)	170	540
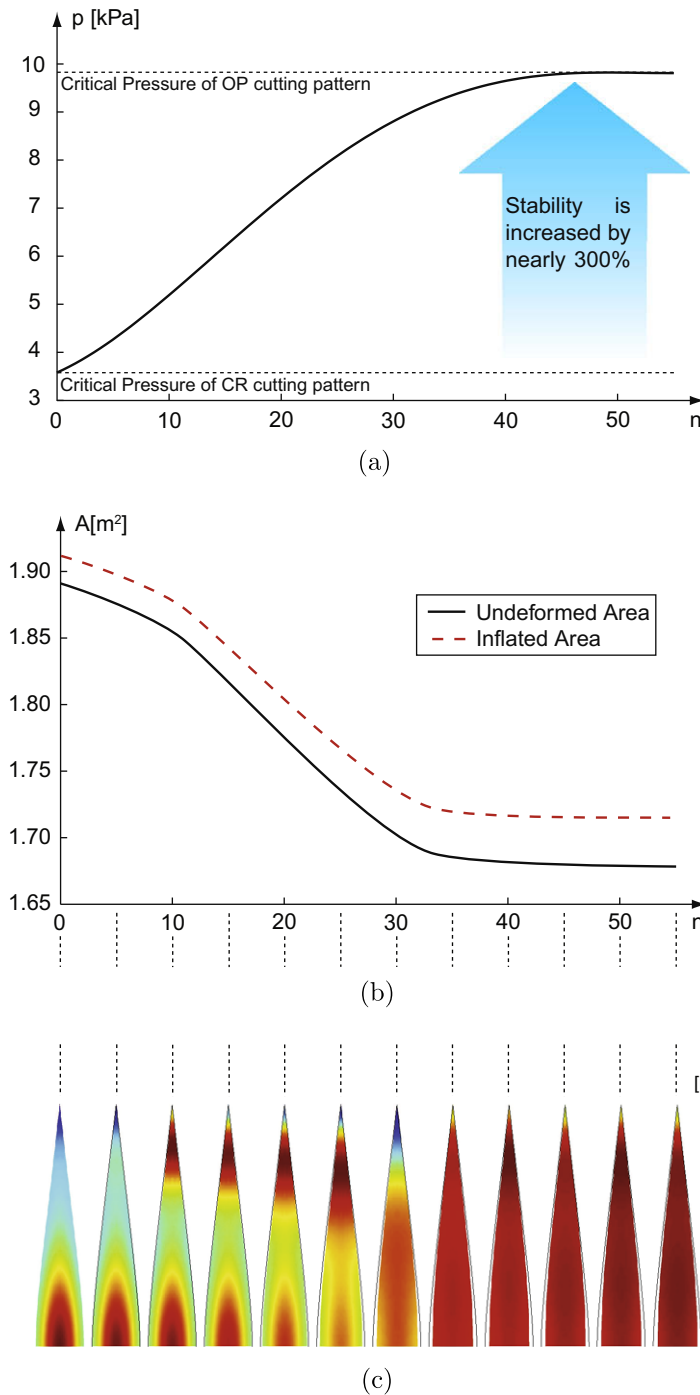
Fig. 8. Optimization history of 10 m diameter balloon with 145 lobes for $n = 55$ iterations: (a) cutting pattern area; (b) buckling pressure; and (c) Mises stresses.

about 40 iterations. Furthermore, the buckling pressure converges to a value that is nearly 300% above the value of the CR cutting pattern with identical maximum film stresses. The maximum Mises stresses as well as the change of the optimization variables during the optimization have been plotted in Fig. 9. Note that of the six variables v_0 to v_5, $v = 0$, v_1 to v_4 have been plotted, and v_5 has been eliminate through symmetry. The major change during the optimization occurs in the variable v_4 that has the largest influence on the width at the equator whereas the other three variables are only modified by a couple of millimeters. It should also be noted that we have chosen for this example a maximum step length $|\Delta \mathbf{v}| = 1$ mm. However, the results presented in this paper are

based on an adaptive step length so that the necessary number of iterations can be considerably decreased.

Fig. 10(a) shows the stress distribution in the cutting patterns of balloons with different number of lobes before and after the optimization. It should be noted that in the figure the width of each CR cutting pattern has been scaled to the same amplitude, and the width of the corresponding optimized (OP) pattern has been scaled proportionally. It can be seen that the stresses in the optimized cutting patterns are nearly uniform. Furthermore, it should be noted that the optimized cutting patterns have a much smaller area than the corresponding CR designs. This effect is especially pronounced for designs with a small number of lobes. For a large
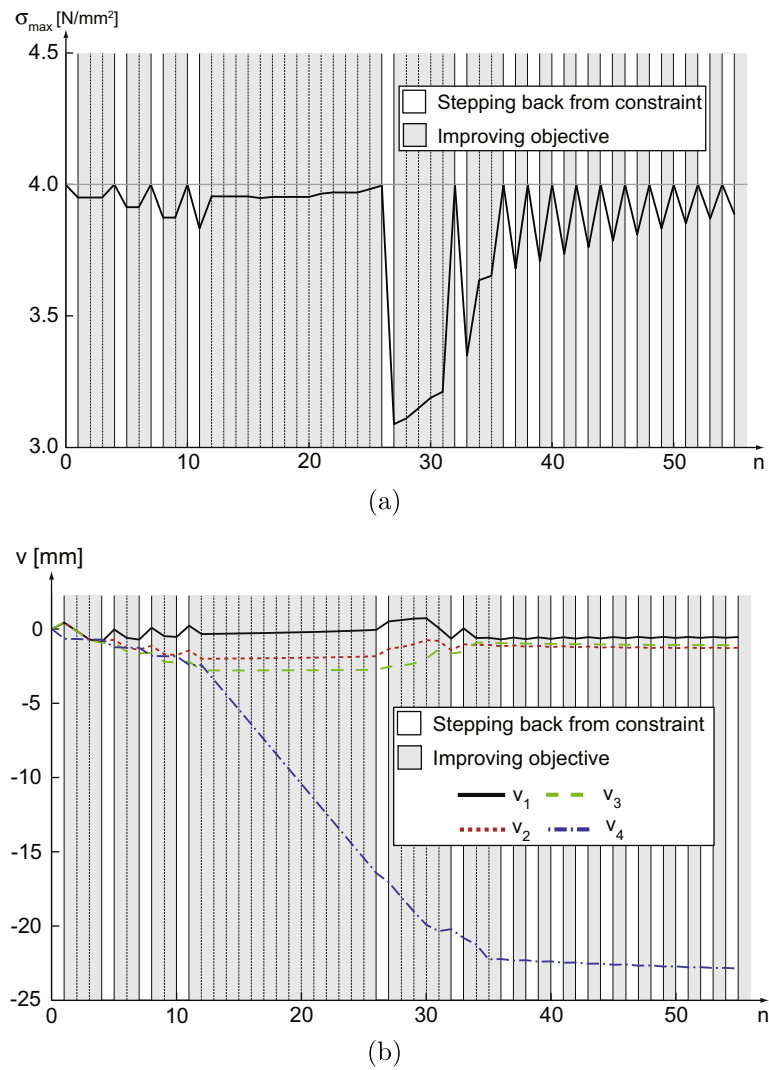
Fig. 9. Optimization history of 10 m diameter balloon with 145 lobes for $n = 55$ iterations: (a) maximum Mises stresses; (b) change of initial optimization variables.
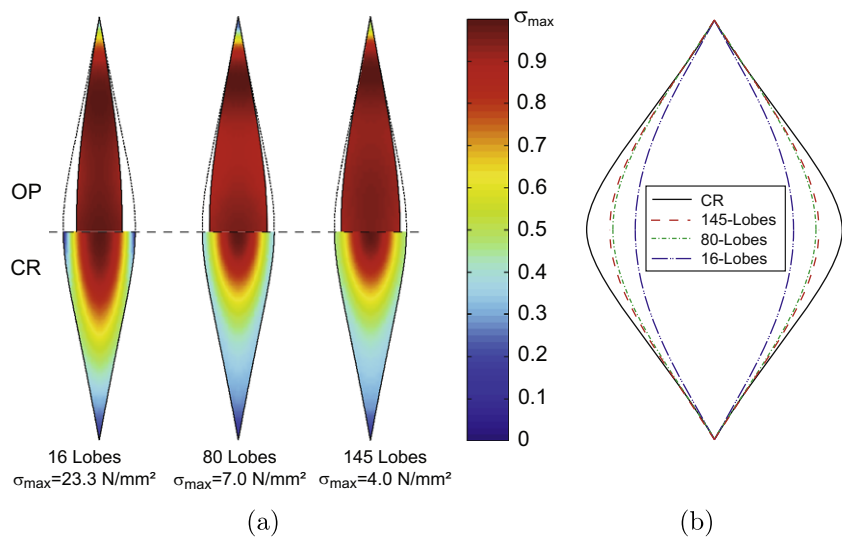

Fig. 10. Comparison between OP and CR cutting patterns of 10 m diameter balloons at $p = 500$ Pa: (a) von Mises stresses; (b) shape of cutting patterns.

number of lobes the width reduction ratio converges to a constant value. This is illustrated in Fig. 10(b) where the scaled cutting patterns are plotted together with a CR design.

Fig. 11 shows the profile of the tendons of balloons with CR and OP cutting patterns. It is interesting to note that the optimized tendons, particularly for the smaller values of n, are closer to a sphere. Since the stresses in the membrane of a 16-lobe balloon with a CR cutting pattern are relatively high the optimization generates a nearly spherical balloon with an optimum ratio of surface area to enclosed volume.

Note that the shapes of lobed balloons with increasing number of lobes, for both CR and OP cutting patterns, converge towards an axisymmetric, unlobed shaped that matches the equilibrium surface that carries a uniform differential pressure purely with meridional stress, i.e. the hoop stress is zero everywhere. This surface is known as the isotensoid.

One reason why it is possible to create cutting patterns with smaller areas and identical maximum membrane stresses than conventional CR designs is because of the large strains that occur at the equator due to the incompatibility between a flat and doubly curved surface. See Pagitz and Pellegrino (2007) for a detailed discussion. The main advantage of a fully stressed design is illustrated in Fig. 12, which shows that the optimized designs are much more stable than their CA and CR counterparts.

6.2. Flight-size balloons

It has been shown for small scale balloons that optimizing the cutting pattern can considerably increase the buckling pressure. This section extends the investigation to flight-size balloons. Fig. 13 shows the Mises stresses of an original and optimized cutting pattern, for a flight-size balloon at $p = 200$ Pa. It can be seen that, as already in the case of the small scale balloons, the Mises stresses are nearly uniform after the optimization. Furthermore, the width of the cutting pattern reduces considerably.

A comparison of the corresponding maximum stresses and cutting pattern areas (A is the unstressed surface area of a given design and A_S is the area of a sphere) before and after the optimization is presented in Table 2. Note that the surface area decreases considerably, as in the previous examples. Another interesting result is that the optimized cutting pattern for a balloon where the tendons are pre-strained during construction results in a balloon with $p_{crit} = 2117$ Pa and a further slight reduction of the total surface area. Hence, the effect that a prestress in the tendons reduces the buckling pressures, observed for CR designs by Pagitz and Pellegrino (2007), is not seen in optimized cutting patterns.

Fig. 14 is a plot of the membrane stresses along the centreline of the gore, for an 80 m diameter CR balloon and its optimized
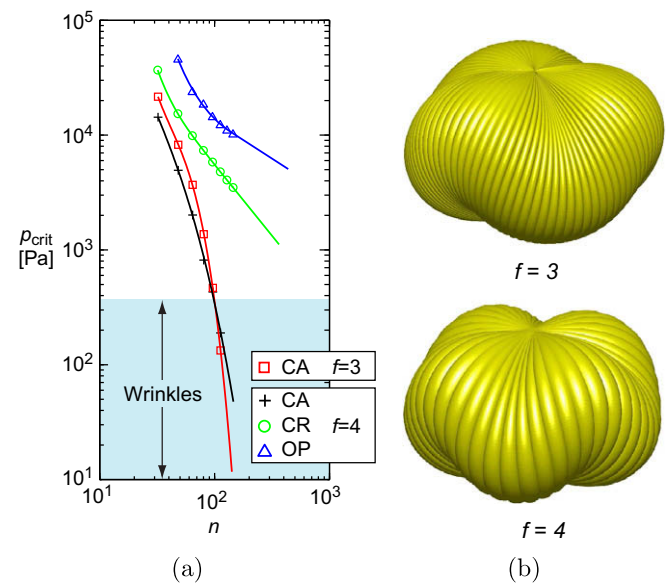
counterpart, at a differential pressure of $p = 200$ Pa. Note that in both cases the maximum Mises stress is 4 N/mm^2, but for the optimized cutting pattern both principal stresses are more uniform along the arc-length. Fig. 15(a) is a plot of variation along the lobe of the ratio between the arc-length of the lob cross-section (measured on the inflated lobe) and its cord-length. This ratio is much smaller for the optimized cutting pattern due to the reduced width. It is interesting to consider also the radius of the inflated lobes, plotted in Fig. 15(b). As expected the CR cutting pattern produces a nearly uniform radius; however, the optimized result is quite different. The reason for the reduction towards the equator is the high longitudinal stresses due to the geometric incompatibility, hence the stresses in the transverse direction have to be reduced in this region by decreasing the radius.

Fig. 16 shows the undeformed and deformed surface areas of balloons for CR and optimized cutting patterns together with the maximum Mises stresses at $p = 200$ Pa as a function of the number of lobes. Again, the optimized cutting patterns have a considerably smaller surface area than the CR designs, at comparable or even smaller maximum Mises stresses. The undeformed surface area of some optimized balloons is even smaller than the area of an isotensoid with identical volume. Note that due to the uniform stress distribution, the pressure-induced increase in surface area of the
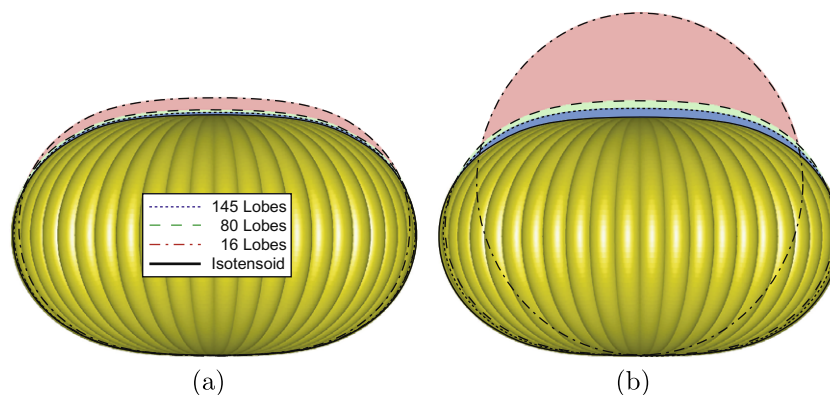

Fig. 12. (a) Buckling pressure versus number of lobes for 10 m diameter balloons with CA, CR and OP cutting patterns; (b) associated mode shapes.

Fig. 11. Tendon profiles for (a) CR and (b) OP cutting patterns of 10 m diameter balloons at $p = 500$ Pa.
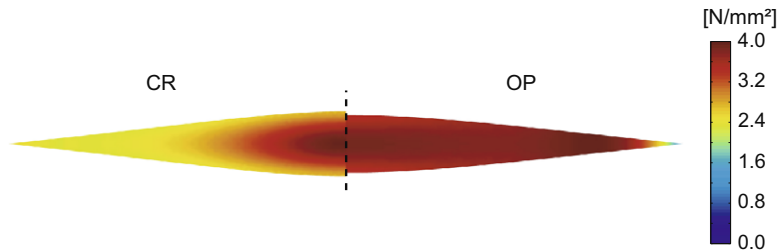
Fig. 13. Mises stresses of CR and OP cutting pattern of 80 m diameter balloon at p = 200 Pa.

Table 2
Comparison of cutting patterns for 80 m diameter balloons.

	Sphere	Isotensoid	CR	OP	OP ($\varepsilon_0 = 0.3\%$)
Volume (m³)	175,731 ($\sim 6mcf$)	40	40	40	40
Radius (m)	34.75	40	40	40	40
Area (m²)	15,180	15,790	17,210	16,070	15,860
$(A - A_S)/A_S$ (%)	0	4.1	13.4	5.9	4.5
Maximum σ_1 (N/mm²)	72.4	∞	4.7	4.4	4.6
Maximum σ_2 (N/mm²)	72.4	0	2.5	3.8	3.6
Maximum Mises stress (N/mm²)	72.4	∞	4.0	4.0	4.0
p_{crit} (Pa)	∞	0	734	1953	2117
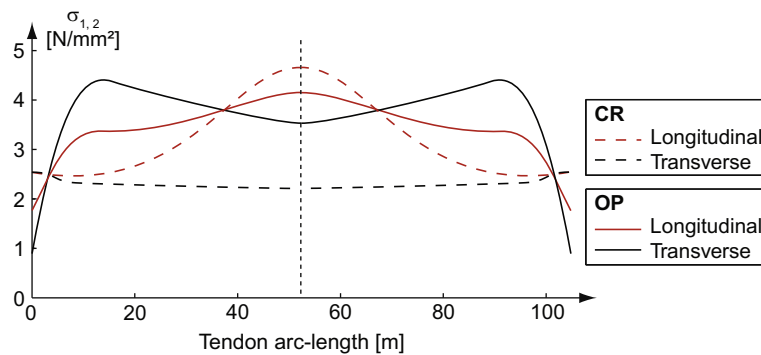
Fig. 14. Principal stresses along lobe centreline for CR and OP 80 m diameter balloon, at p = 200 Pa.
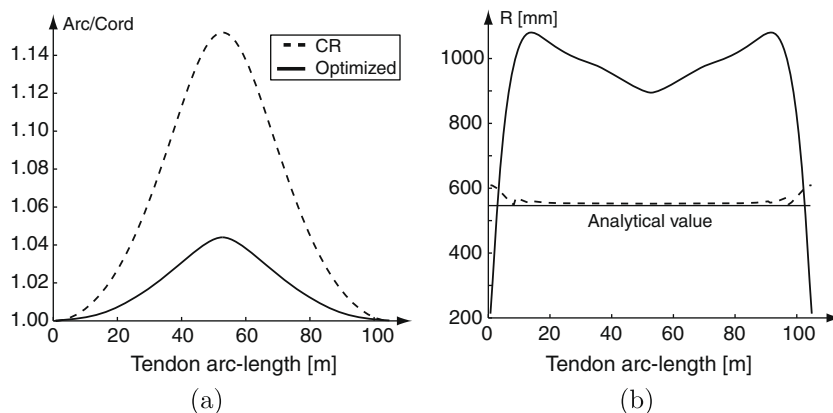

(a)

(b)

Fig. 15. Comparison of CR and OP cutting pattern of 80 m diameter balloon at p = 200 Pa: (a) ratio between arc-length and cord-length; (b) radius.

optimized designs is proportional to the maximum membrane stress. Another nice result is that given a maximum Mises stress the pressurized surface area of the balloons with the smallest possible number of lobes (represented by solid dots in Fig. 16) is roughly constant.

6.3. Thermal loading effects

The manufacturing and operational temperatures of a balloon are different, hence thermal effects need to be taken into account. The thermal coefficient of the tendons is considerably smaller
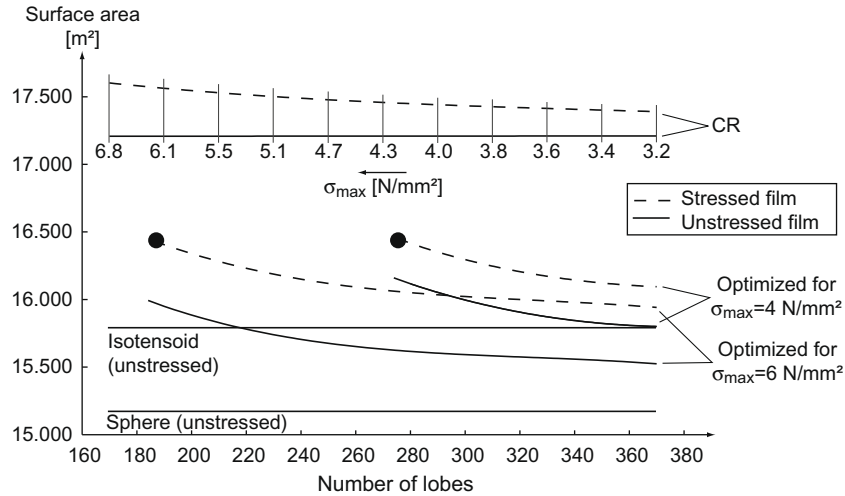
Fig. 16. Unstressed/stressed surface areas of CR and OP 80 m diameter balloons for p = 200 Pa, as a function of number of lobes.

than that of the membrane and hence will be neglected, for simplicity.

A typical temperature to which a balloon is exposed during its mission is $\sim\!-30\,°C$. Assuming a mean temperature during manufacturing of 20 °C the overall temperature change is $\Delta T = -50\,°C$. The effect on the membrane can be modeled by assuming an isotropic prestress of magnitude

$$\sigma_T = \frac{\Delta T \alpha E}{1 - v}, \tag{24}$$

where ΔT is the change of temperature and α is the linear coefficient of thermal expansion. This equation can be derived by computing the stresses that result in a fixed membrane, of any shape, from the thermal strains

$$\varepsilon_1 = \varepsilon_2 = \Delta T \alpha. \tag{25}$$

A new optimized cutting pattern that allows for both a pressure loading of p = 200 Pa and a thermal loading of $\Delta T = -50\,°C$ has been obtained by running the optimization algorithm. Fig. 17 shows the stress distribution along the longitudinal centreline for both the CR lobe and the optimized lobe. It should be noted that, in both cases, the maximum Mises stress is 8 N/mm². It can be seen that, for the optimized cutting pattern, both principal stresses are more uniform along the arc-length. Again, it is found that given the number of lobes it is not possible to arbitrarily reduce the maximum Mises stress in the membrane simply by increasing the width of the lobe cutting pattern. As in the case of the 10 m diameter balloons, the

reason for this is the stress peak at the equator, which has been further increased by the thermal effects.

Fig. 18 compares the shapes of the CR and OP cutting patterns when loaded by p = 200 Pa and ΔT equal to either 0 or =−50 °C. In Fig. 18(a) it can be seen that both cutting patterns become flatter, i.e. the arc/cord-length becomes smaller, when the thermal loading is considered. It can also be seen that the OP pattern leads to a lobe up to 11% flatter although the peak stress is practically the same. Comparing Fig. 18(a) with Fig. 15(a) we see that the cutting pattern optimized for the thermal as well as pressure loading has larger arc/cord-length near the apex of the balloon.

Fig. 19 shows the deformed and undeformed surface areas of balloons with CR and optimized cutting patterns, together with the maximum Mises stresses that occur for p = 200 Pa and ΔT = −50 °C. Again, it is found that the optimized cutting patterns have a considerably smaller surface area than the conventional CR designs, at comparable or even smaller maximum Mises stresses. Due to the thermal effects, this time the inflated surface area is, depending on the number of lobes and stress constraint, smaller than the undeformed area. Therefore, in the plot the dotted lines lie below the solid lines, but again the change of surface area is related to the maximum allowed membrane stresses. Furthermore, the pressurized surface area, for a given maximum Mises stress and the smallest possible number of lobes, is again roughly constant.

Finally, Fig. 20 compares the stress distribution in CR and optimized designs, with and without thermal loading, at a differential pressure of p = 200 Pa. Note that the optimized design re-
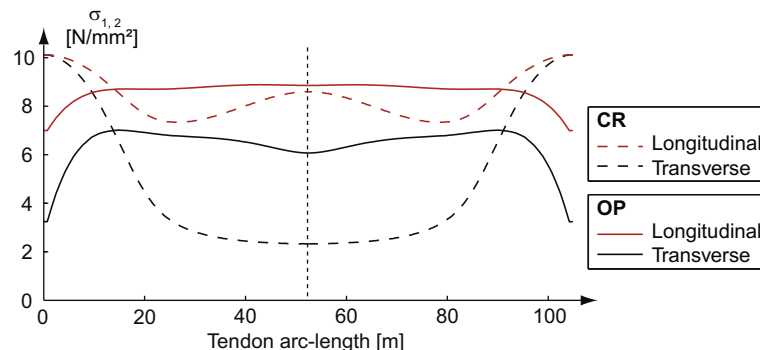

Fig. 17. Principal stresses in longitudinal direction of CR and OP 80 m diameter balloon at 200 Pa and a membrane temperature change of $\Delta T = -50\,°C$.
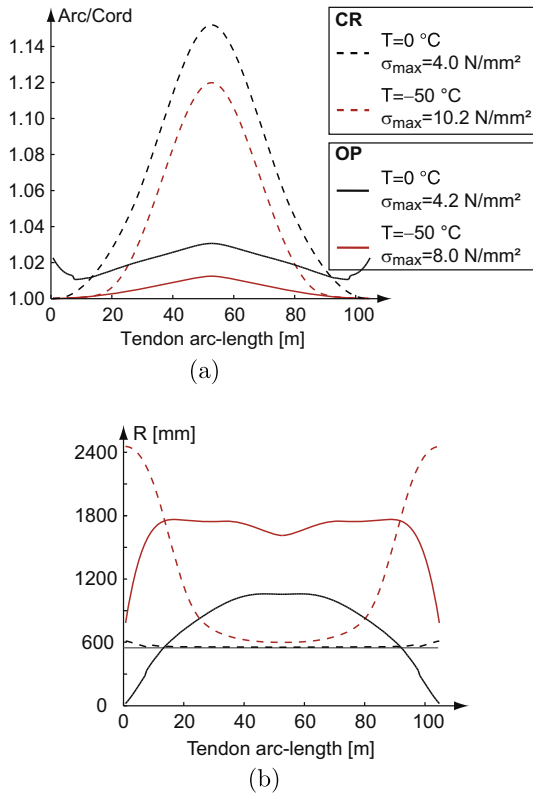
Fig. 18. Comparison of CR and OP cutting pattern for 80 m diameter balloon at $p = 200$ Pa: (a) ratio between arc-length and cord-length; (b) radius.

sults in a relatively uniform stress distribution, both with and without thermal loading. Furthermore, the maximum stress for the thermal loading is smaller than that observed for a standard CR design.

7. Conclusion

It has been shown that the stability of pumpkin balloons can be considerably increased by optimizing the lobe cutting patterns. The maximum stability is reached if the surface area of the optimized lobe is minimized under a given stress constraint which results in a fully stressed design. One of the striking results is that the unstressed surface area is in some cases smaller than the area of an unlobed, axisymmetric surface (isotensoid). This suggests a potential way of eliminating the deployment instability problems that have affected previous lobed super-pressure balloons. Current experimental investigations of this design paradigm involving pumpkin balloons with diameters of 4 m, 27 m and 83 m, are very promising since no instabilities occurred during inflation (Cathey and Pierce, 2007; Hand, 2009; Flynn, 2009).

Throughout this paper it has been assumed that the balloons possess a horizontal symmetry plane at the buckling pressure. This assumption is reasonable since gravity effects on a symmetrically designed balloon are small in comparison to the effects of the critical buckling pressure, but it is by no means essential for the approach presented in this paper. Actual super-pressure balloons often use a reinforcing cap near the top apex to carry the stresses induced by the launch. It would be straightforward to extend our approach by removing the assumption of a symmetric cutting pattern.
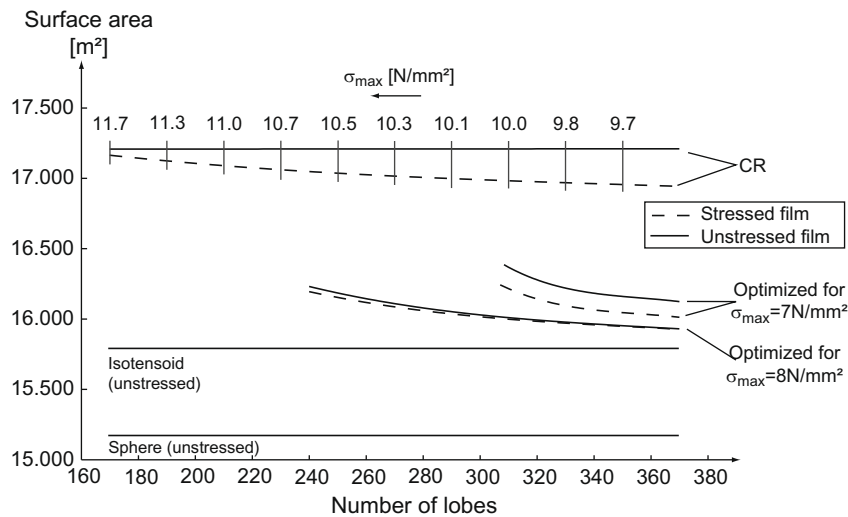

Fig. 19. Unstressed/stressed surface areas of CR and OP balloons for $p = 200$ Pa and $\Delta T = -50$ °C, as a function of number of lobes.
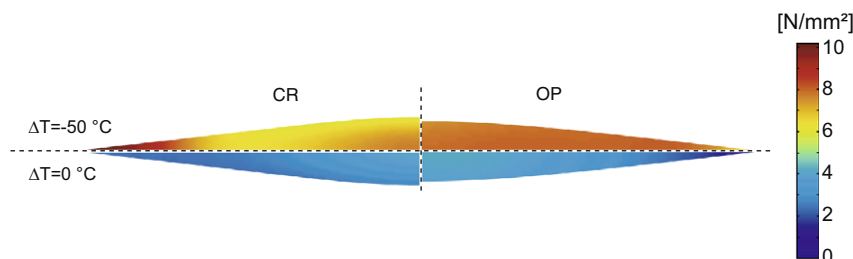

Fig. 20. Stresses in CR and OP cutting patterns for $p = 200$ Pa and $\Delta T = 0, -50$ °C.

Acknowledgments

References

Baginski, F.E., Brakke, K.A., Schur, W.W., 2006. Cleft formation in pumpkin balloons. Advances in Space Research 37, 2007–2081.

Bernstein, S.N., 1912. Démonstration du théorème de Weierstrass fondée sûr le calcul dés probabilités. Communications Society in Mathematics 12, 1–2.

Cathey, H.M., Pierce, D.L., 2007. Development of the NASA ultra-long duration balloon. In: NASA Science Technology Conference, 19–21 June 2007, University of Maryland.

Deng, X., Pellegrino, S., 2008. Computation of partially inflated shapes of stratospheric balloon structures. In: 48th AIAA/ASME/ASCE/AHS/ASC Structures, Structural Dynamics and Materials Conference, 7–10 April 2008, Schaumburg, Illinois, AIAA-2008-2133.

Flynn, E.D., 2009. Antarctic balloon launch lifts research hopes. Aerospace America, 22–25.

Hand, E, 2009. Test balloon breaks endurance record, Nature News, 8 February 2009, doi:10.1038/news.2009.85.

Karush, W., 1939. Minima of functions of several variables with inequalities as side constraints, Department of Mathematics, University of Chicago.

Kuhn, H.W., Tucker, A.W., 1951. Nonlinear programming. In: Proceedings of Second Berkeley Symposium.

Pagitz, M., Pellegrino, S., 2007. Buckling pressure of pumpkin balloons. International Journal of Solids and Structures 44, 6963–6986.

Press, W.H., Teukolsky, S.A., Vetterling, W.T., Flannery, B.P., 2003. Numerical Recipes in C++. Cambridge University Press, Cambridge.

Rand, J.L., Sterling, W.J., 2006. A constitutive equation for stratospheric balloon materials. Advances in Space Research 37 (11), 2087–2091.

Schur, W.W., 2004. Experimental investigation of undesired stable equilibria in pumpkin shape super-pressure balloon designs. Advances in Space Research 33, 1682–1687.

Schur, W.W., Jenkins, S.H., 2002. Deployment destiny, stable equilibria, and the implications for gossamer design. In: 43rd AIAA/ASME/ASCE/AHS/ASC Structures, Structural Dynamics, and Materials Conference, 22–25 April 2002, Denver, Colorado, AIAA-2002-1205.

Vanderplaats, G.N., 2001. Numerical Optimization Techniques For Engineering Design. Vanderplaats Research & Development, Inc..

Zoutendijk, G., 1960. Methods of Feasible Directions. Elsevier, Amsterdam.